

## Article

# Deep Eutectic Solvent-Mediated Synthesis of $\text{Ni}_3\text{V}_2\text{O}_8/\text{N}$ -Doped RGO for Visible-Light-Driven $\text{H}_2$ Evolution and Simultaneous Degradation of Dyes

Fahad A. Alharthi <sup>\*</sup>, Alanood Sulaiman Ababtain , Hend Khalid Aldubeikl, Hamdah S. Alanazi and Imran Hasan <sup>\*</sup> 

Department of Chemistry, College of Science, King Saud University, Riyadh 11451, Saudi Arabia

<sup>\*</sup> Correspondence: fharthi@ksu.edu.sa (F.A.A.); iabdulateef@ksu.edu.sa (I.H.)

**Abstract:** Photochemical hydrogen evolution and the degradation of synthetic dyes in water are the two key ways to unravel the issues associated with the energy and environmental sectors for sustainability. The present work deals with the use of a deep eutectic solvent for the synthesis of  $\text{Ni}_3\text{V}_2\text{O}_8/\text{N}$ -doped reduced graphene oxide (NiV/NR hybrid). The NiV/NR hybrid, NRGO, and NiV were characterized using XRD, SEM, TEM, UV-DRS, XPS, and other photo-electrochemical techniques. The NiV/NR hybrid exhibited high efficiency towards light-driven hydrogen evolution (12,546  $\mu\text{mol}$ ) compared to pristine NiV (6453  $\mu\text{mol}$ ) and NRGO (1935  $\mu\text{mol}$ ). Among the various sacrificial agents examined, TEOA showed better activity in  $\text{H}_2$  evolution. The photocatalytic degradation of anionic (Methyl orange; MO) and cationic dyes (crystal violet; CV) were evaluated and the reaction conditions were carefully optimized to attain the utmost efficiency. The efficiency of the NiV/NR hybrid was higher under visible light irradiation than UV light and able to degrade 94.6 and 96.7% of MO and CV, respectively. The results of the simultaneous degradation of dyes and total organic carbon (TOC) removal were good. Based on the obtained bandgap and Mott-Schottky plots, the mechanism of photocatalysis in the NiV/NR hybrid is discussed in detail. The reusability and stability of the NiV/NR hybrid in both  $\text{H}_2$  evolution experiments and degradation studies are excellent. The fabricated NiV/NR hybrid material could be used for multiple applications in energy and environmental applications.

**Keywords:** deep eutectic solvent; NiV/NRGO;  $\text{H}_2$  evolution; simultaneous dye degradation; photocatalysis



**Citation:** Alharthi, F.A.; Ababtain, A.S.; Aldubeikl, H.K.; Alanazi, H.S.; Hasan, I. Deep Eutectic Solvent-Mediated Synthesis of  $\text{Ni}_3\text{V}_2\text{O}_8/\text{N}$ -Doped RGO for Visible-Light-Driven  $\text{H}_2$  Evolution and Simultaneous Degradation of Dyes. *Inorganics* **2023**, *11*, 67. <https://doi.org/10.3390/inorganics11020067>

Academic Editors:  
Alejandro Pérez-Larios and Oomman K. Varghese

Received: 23 December 2022  
Revised: 21 January 2023  
Accepted: 26 January 2023  
Published: 31 January 2023



**Copyright:** © 2023 by the authors. Licensee MDPI, Basel, Switzerland. This article is an open access article distributed under the terms and conditions of the Creative Commons Attribution (CC BY) license (<https://creativecommons.org/licenses/by/4.0/>).

## 1. Introduction

Industrialization, urbanization, and lifestyle upgrades by people across the globe lead to an enormous amount of issues related to energy and the environment [1,2]. The demand for other energy sources is high due to pollution and the shortage of fossil fuels in the near future. The energy demand at present and in the future will be met through alternate sources of energy such as  $\text{CO}_2$  utilization, solar cells, bio-ethanol,  $\text{H}_2$  gas, etc. [3,4]. Therefore, efficient hydrogen evolution is one way to address the scarcity associated with the energy sector. Hydrogen is green, clean energy that is manufactured using Ru and Pt catalysts, which are not economical and not easily available [5]. Semiconductors that can split water and generate hydrogen in the presence of light are gaining much importance due to their abundance and ease of handling [6,7].

On the other hand, environmental pollution is another major issue that requires much attention to maintain the ecological balance. Water gets contaminated due to the accumulation of heavy metals, dyes, pharmaceuticals, personal care products, pesticides, preservatives, etc. [8]. Synthetic dyes are being used in the textile, leather, pharmaceutical, and hair color manufacturing industries, which are the main sources of water pollution [9,10]. Synthetic dyes exhibit high stability due to their aromatic nature and will not undergo degradation for a longer time. Meanwhile, the accumulation of the dyes in water causes

an imbalance in the livelihood of aquatic life and affects photosynthesis in plants. Methyl orange (MO) is an anionic dye, and crystal violet (CV) is a cationic dye used excessively in the manufacturing sector that later accumulates in water as a pollutant and stays for a longer time [11,12]. Hence, these dyes are to be removed from the water to avoid severe health issues. Dye removal has been achieved through many methods, such as adsorption, ion exchange, membrane separation, coagulation, photocatalytic degradation, etc. Photocatalysis is a different and promising technique since it not only removes dyes but also degrades them into less harmful products [13,14].

Many semiconductor metal oxides such as NiO, ZnO, Ta<sub>2</sub>O<sub>5</sub>, TiO<sub>2</sub>, V<sub>2</sub>O<sub>5</sub>, and BiVO<sub>4</sub> have been extensively used for photocatalytic hydrogen evolution and the degradation of dyes [15–17]. Metal vanadates are gaining high importance due to their non-cytotoxicity, mixed oxidation states, availability of oxygen vacancies, enhanced stability, and ease of bandgap engineering. Hence, metal vanadates are finding their applications in Li-ion batteries, supercapacitors, sensors, photocatalysis, etc. due to their versatile geometry and presence of multiple oxidation states [18–24]. Metal vanadates are binary metal oxides that occur in different forms: ABO<sub>4</sub>, AB<sub>2</sub>O<sub>4</sub>, and A<sub>3</sub>B<sub>2</sub>O<sub>8</sub>, where A stands for any metal (Fe, CO, Ni, Bi, Sm), and B stands for vanadium. Vanadium is an abundantly available metal and exhibits variable oxidation states (3 to 5). Ni<sub>3</sub>V<sub>2</sub>O<sub>8</sub> has been used for photocatalytic degradation studies [25–28]. Still, NiV exhibits its limitations of fast recombination of electrons and holes, low conductivity, and low visible light assimilation. Hence, it is preferred to decorate NiV with other carbon-based materials, metal oxides, etc.

The graphene-related layered materials are one of the ideal selections for generating the hybrid structure of NiV. Graphene exhibits a semimetal nature, Sp<sup>2</sup> hybridization with zero bandgap, enhanced surface area, flexibility, and excellent electrical conductivity. Reduced graphene oxide (RGO) is a type of graphene that has strong blending capabilities with other metal oxides, vanadates, and sulphides [29–31]. Heteroatom doping is one of the promising ways to enhance the electrochemical or catalytic activity of RGO. The carbon in the RGO could be easily replaced by N, B, and S atoms. Nitrogen doping of the RGO matrix has resulted in superior performances due to the generation of defects and the increased availability of electrons [32].

NiV/graphene-based materials were synthesized by using the reflux method, ultrasonic, sol-gel, solvothermal, and high-temperature solid-state methods [23–25,33,34]. The synthesis of NiV/N-doped RGO (NiV/NR) hybrid material has not been explored through the deep eutectic solvent (DES) method. The advantages of using DESs are their economy, non-toxicity, and ease of accessibility.

The authors of the present work synthesized NiV, NRGO, and NiV/NR hybrid materials using a facile deep eutectic solvent method. The synthesized materials were characterized by their morphological, structural, and photoelectrochemical properties. NiV/NR exhibited high performance towards photocatalytic hydrogen evolution and degradation of MO and CV dyes. The NiV/NR hybrid was also evaluated for simultaneous degradation of dyes, total organic carbon removal and stability studies. The results imply the efficient photocatalytic behavior of the NiV/NR hybrid with good stability and ability towards energy and environmental remediation.

## 2. Results and Discussion

### 2.1. Structural and Morphological Characterization

XRD studies are used to determine the crystal structure and the crystal size of the synthesized materials. The XRD patterns of the NRGO, NiV, and NiV/NR are shown in Figure 1. The peaks for pure NRGO are in the 2θ position at 24.6 and 43.2°, which correspond to the 002 and 100 crystallographic planes. The XRD pattern of NiV consists of many peaks at 2θ position 19.15, 25.49, 31.31, 33.91, 36.14, 37.32, 38.33, 40.51, 43.82, 54.83, 60.50, and 64.31 assigned to (020), (120), (200), (220), (211), (231), (131), (122), (151), (242), (162), and (004) diffraction planes, respectively. These observed peaks are indexed according to the orthorhombic phase of NiV according to JCPDS card no. 74-1484 [28]. The

XRD patterns of the NiV/NR hybrid show retained peaks of both NRGO and NiV, but the intensity of the peaks related to NiV is reduced, and a slight shift in the peak positions are observed. No additional peaks are observed in the hybrid material, indicating the absence of impurities.

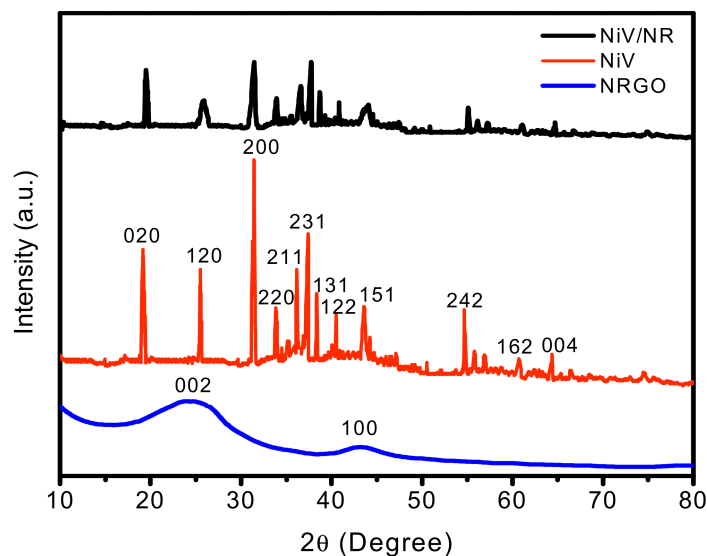


**Figure 1.** The X-ray diffraction patterns of NRGO, NiV, and the NiV/NR hybrid.

The Raman spectra of NRGO, NiV, and NiV/NR are shown in Figure S1. The Raman spectra of the NRGO exhibit the presence of D and G bands at around  $1587\text{ cm}^{-1}$  and  $1332\text{ cm}^{-1}$ , respectively. The bond V-O in NiV has asymmetric stretching vibrations, which cause the weak peak at  $794\text{ cm}^{-1}$ . These results further confirm the formation of the NiV/NR hybrid.

Surface morphology characterization of the materials was conducted using SEM and TEM techniques. The SEM image of the NRGO (Figure 2a) shows the presence of layered and also wrinkled structures. This was further confirmed by the TEM image, which shows the well-distributed layered structure with some dark patches on its surface that may be due to the incorporation of nitrogen into its matrix (Figure 2b). The micrograph of NiV in Figure 2c shows the formation of some irregular disk-shaped particles that are distributed unevenly, and also, we may be able to distinguish the presence of different contrast in the image that may be due to the presence of two different metal atoms present. The EDX spectra of the NiV/NR hybrid are displayed in Figure S2. The presence of nickel, vanadium, carbon, and oxygen can be seen prominently in the spectra. Since the spectra show no traces of other impurities, the sample must be pure. Table S1 gives the % weight of elements presents in the NiV/NR hybrid. Insight into this morphology is shown by TEM (Figure 2d), which is able to show the presence of almost hexagonal disc-shaped particles. Figures 2e and 2f, respectively, show the SEM and TEM micrographs of the NiV/NR hybrid. The SEM image shows the formation of the unevenly layered structure and the anchoring of various sizes of NiV particles that are completely distributed on the NRGO surface. The functional groups on the surface of NRGO that included oxygen may have been eliminated and may now have significant van der Waals interactions between metal atoms and graphene layers. This resulted in the graphene structure becoming wrinklier and curlier, creating the lamella structure. The NRGO was relatively transparent and consistently and thickly covered in NiV particles, according to the TEM image.

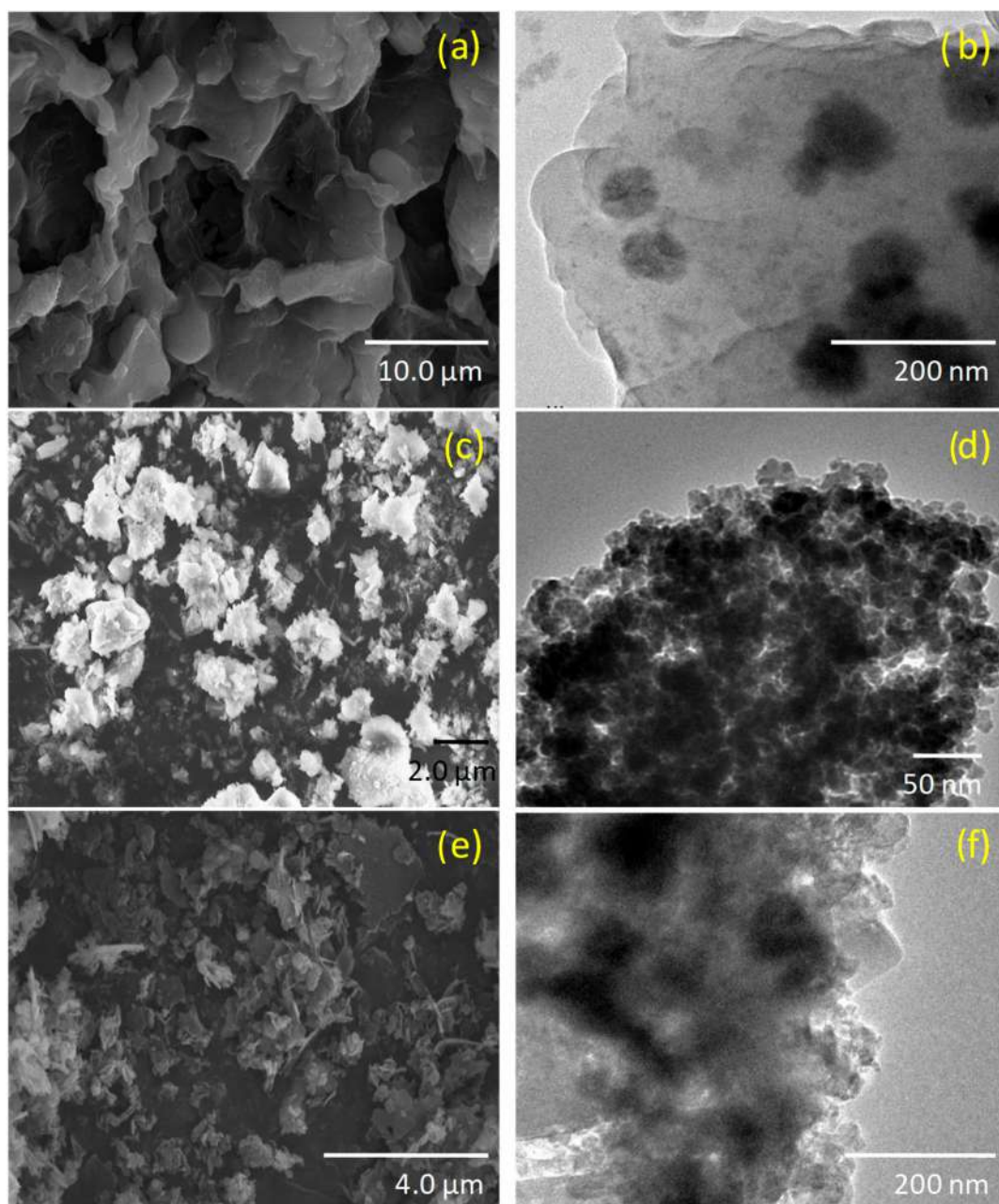


**Figure 2.** SEM and TEM monographs of (a,b) NRGO, (c,d) NiV, and (e,f) the NiV/NR hybrid.

The successful anchoring of NiV to NRGO and the oxidation states of the elements present in the hybrid material are further evaluated using X-ray photoelectron spectroscopy (XPS) studies. Figure 3a is the survey spectrum of the NiV/NR hybrid, indicating the presence of only Ni, V, O, N, and carbon without any other elements showing the absence of impurities. Figure 3b depicts the high-resolution XPS of Ni, consisting of two major peaks at binding energies of 854.63 and 872.7 eV assigned to  $2p_{3/2}$  and  $2p_{1/2}$ , respectively. Other two shake-up satellite minor peaks at 861.59 and 879.40 eV are also observed. These four observed peaks of Ni imply the presence of a  $Ni^{+2}$  state [35]. The XPS of V2p is given in Figure 3c and consists of two major peaks at 517.26 ( $2p_{3/2}$ ) and 524.35 ( $2p_{1/2}$ ) eV, which indicate the occurrence of the  $V^{5+}$  state [36]. Two deconvoluted peaks at 530.93 and 532.38 eV for O 1s (Figure 3d) were assigned to the  $-OH$  and  $M-O$  bonds. Three deconvoluted peaks at 284.32 (C-C), 285.30 (C=N) and 288.9 eV (C-N) could be visualized in Figure 3e and belong to the C 1s spectrum. The N 1s XPS spectrum is given in Figure 3f, consisting of three deconvoluted peaks (398.42, 400.31 and 402.18) assigned to pyridinic, pyrrolic, and

graphitic nitrogen, respectively [32]. The results of XPS indicate the doping of N to RGO and the successful formation of NiV/NR hybrid material.

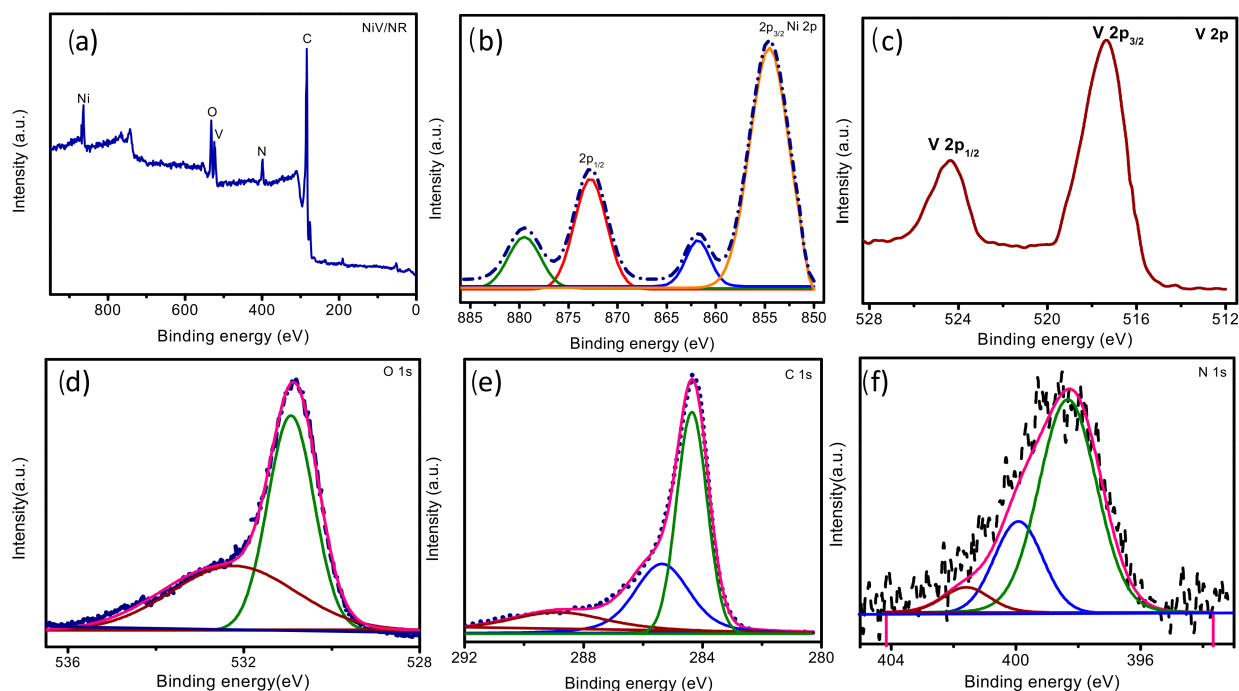


**Figure 3.** XPS of (a) the NiV/NR hybrid survey spectrum (b) Ni 2p, (c) V 2p, (d) O 1s, (e) C 1s and (f) N 1s.

## 2.2. Optical and Photo/Electrochemical Properties

The optical properties of NiV and NiV/NR hybrid materials were examined using UV-DRS. Figure 4a shows the absorption spectrum of NiV, which exhibits the absorption edge at ~540 nm and is later found to shift to the higher wavelength in NiV/NR hybrids at ~600 nm. The enhanced ability in NiV/NR hybrid to absorb light in the visible region is a preferential characteristic in photoredox reactions. The corresponding bandgap was estimated using the Kubelka–Munk theorem, as shown in Figure 4b [37]. The bandgap ( $E_g$ ) of NiV was found to be 2.09 eV and decreased upon anchoring it with NRGO. The bandgap of NiV/NR hybrids is 1.92 eV; a decreased bandgap could help in enhanced photocatalytic activity through successive separation of charge carriers. Further insight into the edge potentials of NiV and the NiV/NR hybrid was obtained through the Mott–Schottky method (Figure 4c). The slopes of the plot insist on the n-type semiconductor. The conduction band edge potentials ( $E_{CB}$ ) of NiV and the NiV/NR hybrid are found to be  $-0.21$  and  $-0.36$  V. By using these obtained results, the valence band edge potential ( $E_{VB}$ ) could be estimated easily by considering  $E_g = E_{VB} - E_{CB}$  formula [38].

The photoelectrochemical properties of the synthesized materials were examined using a time-resolved photocurrent experiment. Figure 4d shows the photocurrent response is in the order NiV/NR > NiV > NRGO. The NiV/NR hybrid exhibited relatively high current density compared to the other two, which indicates the efficient separation of photoexcited electrons and holes [39]. The charge transfer ability of the prepared photocatalysts was further estimated by photoluminescence (PL) spectroscopy (Figure 4e). Low emission peak intensity and a slight shift towards higher wavelengths are observed in the NiV/NR hybrid, which indicates the effective separation of electrons and holes during photoredox reactions. Electrochemical impedance spectroscopy (EIS) studies were evaluated to understand the charge transfer resistance in the samples, and the plot is given in Figure 4f. The NiV/NR hybrid exhibits low arc radius and, hence, high charge transfer ability and low charge transfer resistance [40]. The optical, photo/electrochemical characterization results indicate the enhanced characteristics of NiV upon anchoring it with NRGO for efficient photocatalysis.

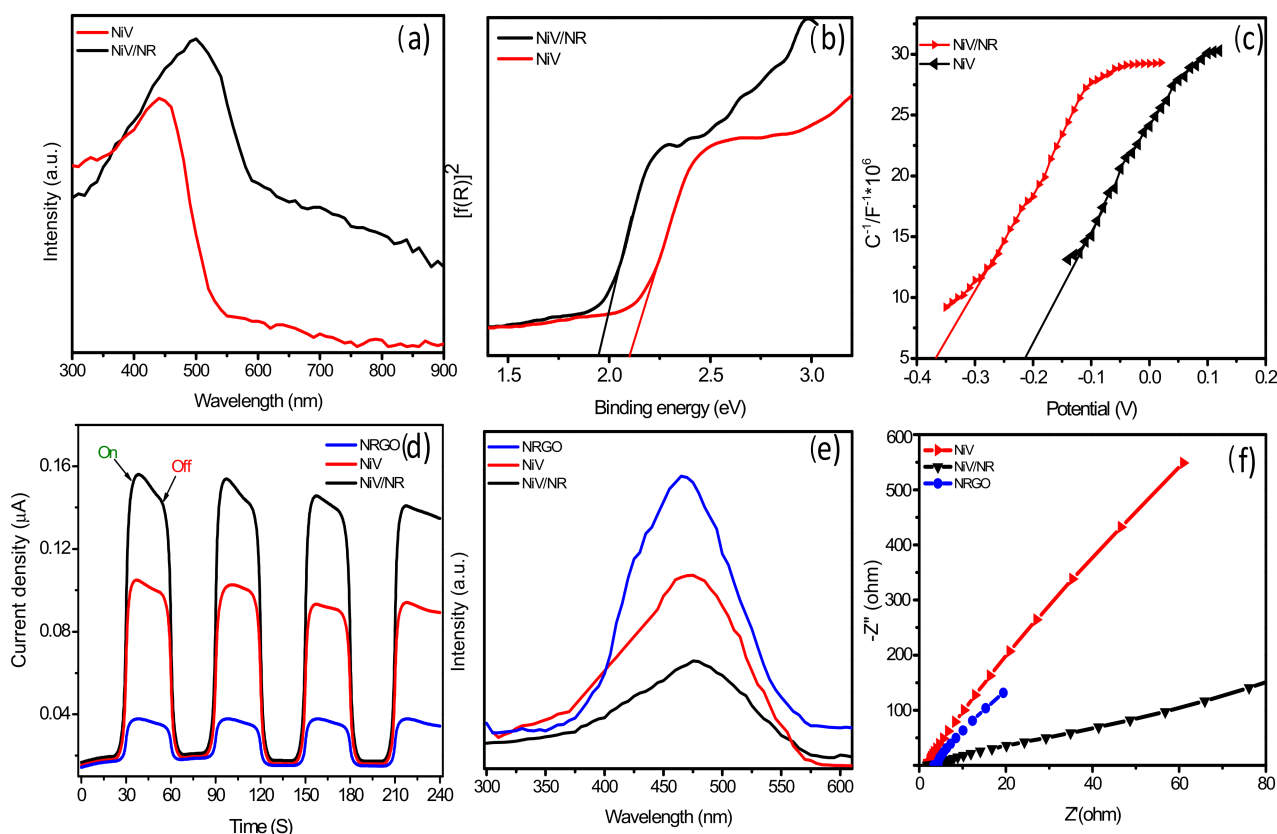


**Figure 4.** (a) UV-DRS spectra; (b) Kubelka–Munk curves; (c) Mott–Schottky plots; (d) Transient photocurrent response; (e) Photoluminescence spectra; (f) EIS analysis.

### 2.3. Photochemical H<sub>2</sub> Evolution

Visible light-driven hydrogen evolution has been evaluated for the synthesized NRGO, NiV, and NiV/NR hybrid materials. The amount of hydrogen that evolved under different conditions is depicted in Figure 5a. The results show that hydrogen evolution cannot take place in dark conditions and the absence of catalysts. Hence, the H<sub>2</sub> evolution reaction is occurring in the system only due to the presence of a catalyst and light. Enhanced ability towards light-driven H<sub>2</sub> evolution is observed in NiV/NR hybrid material (12,546 μmol) compared to NiV (6453 μmol) and NRGO (1935 μmol). The photocatalytic hydrogen evolution efficiency in the NiV/NR hybrid is almost two times and six times greater than that in NiV and NRGO, respectively. Enhanced conductivity and a decreased bandgap in NiV/NRGO increase the easy mobility of electrons and decrease charge carrier recombination during the photoredox process in the presence of the sacrificial agent.

Sacrificial agents used for photocatalysis play an important role in efficient H<sub>2</sub> evolution. Therefore, different sacrificial agents that are commonly used have been evaluated in the presence of the NiV/NR hybrid and the results are given in Figure 5b. No activity is seen in a system consisting of only water, indicating the major role played by sacrificial agents. Less activity is observed in the presence of lactic acid (LA), polyethylene glycol (PEG), and ethylene glycol (EG). A good amount of H<sub>2</sub> evolution is observed in the presence of MeOH, EtOH, and isopropyl alcohol (IPA). Better activity toward the evolution of H<sub>2</sub> is observed in TEOA. Increased H<sub>2</sub> evolution is observed in the TEOA-water system, which could be attributed to the effective dispersion and binding of TEOA to the NiV/NR hybrid [41]. To know the ability to evolve H<sub>2</sub> for a longer time, stability studies of the NiV/NR hybrid have been examined and are given in Figure 5c. No deviation is observed in the first two runs. The third and fourth runs exhibit a slight decline in activity due to a lowered concentration of the sacrificial agent. A fresh sacrificial agent was added after the 4th run and the activity was normal. This indicates the good stability of the NiV/NR hybrid.

The apparent quantum yields (AQYs) were determined using a 420-nm bandpass filter and calculated using Equation (2). The AQY of the NiV/NR hybrid is found to be 5.91% (Figure 5d) and shows good efficiency towards the absorption of light in the visible region.

$$\text{AQY (\%)} = 2 \times \frac{\text{The number of H}_2 \text{ evolved}}{\text{the number of incident photons}} \times 100 \quad (1)$$

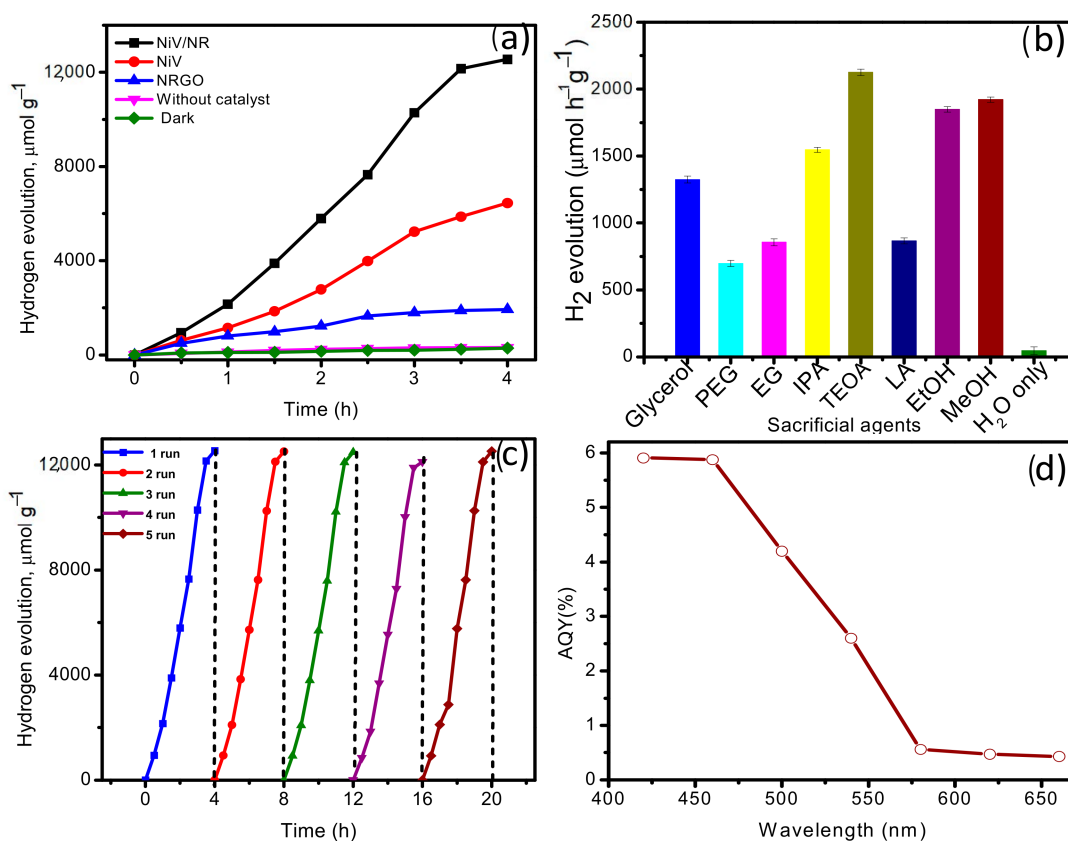


**Figure 5.** (a) H<sub>2</sub> evolution, (b) Effect of sacrificial agents, (c) Stability studies of the NiV/NR hybrid, and (d) AQY of the NiV/NR hybrid.

#### 2.4. Photocatalytic Degradation of Dyes

The removal of synthetic organic dyes from water is an important aspect of environmental remediation, especially through a photocatalytic approach. Methyl orange (MO; anionic) and crystal violet (CV; cationic) dyes were used as model pollutants to evaluate the degradation ability of the synthesized materials. MO and CV dyes were subjected to degradation under different conditions, and the results are represented in Figure 6a. Almost nil degradation was observed under dark conditions. Low activity is observed for NRGO towards the degradation of MO and CV in the presence of both UV and visible light. This shows the ability to absorb radiation in RGO upon doping it with nitrogen. Slightly higher activity is observed in NiV under both UV and visible light sources, indicating its semiconductor behavior. Still, the activity of NiV towards MO and CV degradation is not satisfactory due to the recombination of holes and electrons. In the presence of the NiV/NR hybrid the photocatalytic activity is very high and is able to degrade 96.7 and 94.6% of CV and MO, respectively, under visible light. The enhanced activity in NiV/NRGO could be attributed to the decreased recombination of electrons and holes, enhanced visible light assimilation, and increased conductivity.

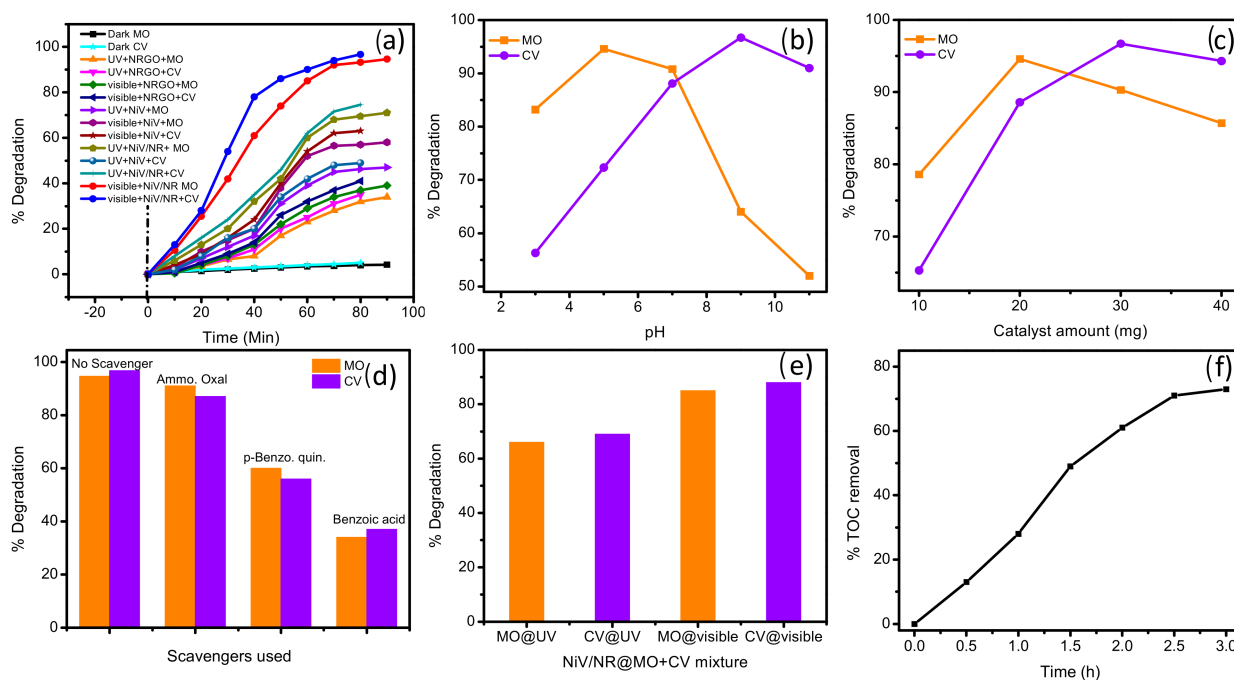


**Figure 6.** (a) Degradation of MO and CV under different conditions; (b) the effect of pH; (c) the effect of the amount of the catalyst; (d) scavenger studies; (e) simultaneous degradation of MO and CV; (f) TOC % removal studies.

Photocatalysis is a multistep reaction that depends mainly on the medium in which it occurs, i.e., the pH of the solution. Figure 6b depicts the effect of pH on the degradation of MO and CV in the presence of the NiV/NR hybrid under visible light. The maximum degradation observed is at acidic pH (pH-5) for MO and basic pH (pH-9) for CV. Being an anionic dye, MO shows a very good electrostatic force of attraction at acidic pH due to the availability of excess H<sup>+</sup> ions. At the same time, in basic pH, due to the repulsions of both the hydroxyl ions and dye, the degradation observed is low. In contrast, the cationic dye (CV) exhibited greater degradation in an alkaline pH since it is drawn electrostatically towards the surface of the catalyst and the generation of a high amount of hydroxyl ions. The amount of catalyst required to degrade the fixed amount of dye concentration is also an important factor for practical applications. The amount of catalyst varied from 10 to 40 mg for degradation of MO and CV under visible light (Figure 6c). It is found that 20 mg and 30 mg are required for efficient degradation of MO and CV, respectively. More than 20 and 30 mg of the Ni/NR hybrid for degradation of MO and CV was found to decrease the efficiency due to inactivation of the catalyst surface due and improper penetration of the light. A scavenger study was conducted to know the reactive species responsible for the degradation of MO and CV. Figure 6d shows the effect of different scavengers for holes (ammonium oxalate), superoxide radicals (p-benzoquinone) and hydroxyl radicals (benzoic acid) upon degradation of MO and CV in presence of NiV/NR [42]. The result shows the order of reactivity  $\bullet\text{OH} > \bullet\text{O}^- > \text{h}^+$ . The involvement of holes is less, and hydroxyl radicals and superoxide radicals are the main reactive species responsible for the degradation of MO and CV.

Industrial effluent usually consists of a variety of pollutants, which may be anions or cations, heavy metals, etc. So, it is required for a photocatalyst to degrade different organic molecules simultaneously. Hence, the simultaneous degradation of MO and CV has been evaluated. A model solution was prepared by mixing 1:1 MO and CV and evaluating the degradation of the resultant mixture. The conditions used were 25 mg of NiV/NR, a pH of 7, UV, and visible light sources, and the absorbance at their respective wavelengths was. Figure 6e shows a degradation of 66 and 69% of MO and CV, respectively, under UV light. Whereas enhanced degradation is found under visible light, observed

degradation was 85 and 89% of MO and CV, respectively. These results show the ability of the NiV/Nr hybrid to degrade different organic molecules in the presence of light. To support the efficient degradation of MO and CV, total organic carbon (TOC) removal study was conducted, and the result is given in Figure 6f. A total of 73% of the total organic carbon has been removed from the MO and CV mixture in the presence of NiV/NR and visible light. The % TOC removal speaks about the effective and efficient mineralization of the organic molecules into less harmful products. The obtained results show high efficiency of the NiV/NR hybrid over many related reports in the literature, as given in Table 1 [27,28,34,43,44].

**Table 1.** Comparison of photocatalytic efficiency of NiV/NR with other related reported works.

Sl No.	Material	Pollutant	Time, min	Efficiency, %	H <sub>2</sub> Evolution	Reference
1	g-C <sub>3</sub> N <sub>4</sub> /Ni <sub>3</sub> V <sub>2</sub> O <sub>8</sub>	Tetracycline HCl	40	97.5	–	[27]
2	V <sub>2</sub> O <sub>5</sub> @Ni <sub>3</sub> V <sub>2</sub> O <sub>8</sub>	Tetracycline HCl	150	90	–	[28]
3	NiVO <sub>4</sub> /BiVO <sub>4</sub>	Acid Orange 7	60	87	–	[34]
4	Ni doped V <sub>2</sub> O <sub>5</sub>	Rhodamine B	100	100	–	[43]
5	Nickel vanadate	Azure B	180	NA	–	[44]
6	NiV/NR	Methyl orange Crystal violet	100 80	94.6 96.7	12,546 μmol	This work

### 2.5. Mechanism of Photocatalysis

Photocatalytic degradation is a multistep reaction that involves many factors such as bandgap, edge potentials, reactive species involved, and conductivity. Based on the UV-DRS, Mott–Schottky, and scavenger study results, a probable mechanism has been predicted and given in Figure 7a. The conduction band ( $E_{CB}$ ) potential of NiV and NiV/NR hybrid follows n-type semiconductors and is considered to be  $-0.31$  and  $-0.46$  V, respectively. The active material is NiV, which can absorb light radiation and undergo excitation. The excited electrons may immediately recombine, and hence the photocatalytic degradation ability in NiV is less. Despite the fact that the bandgap of NiV is 2.2 eV, its efficiency towards dye degradation (MO and CV) is insufficient due to the quick recombination of holes and electrons. NiV is adorned with N-doped RGO to increase its efficiency. RGO is a stable, flexible, and highly conductive material that acts as a channel for electron mobility. Doping N into the RGO matrix is simple and improves RGO activity by producing defects in the matrix, and the lone pair of electrons in the heteroatom N may also play a role in the photoredox reaction. When NRGO is connected to NiV, the excited electrons at NiV are carried away by the N-doped RGO, lowering charge carrier recombination and thereby increasing NiV's photocatalytic efficiency. This leads to the generation of superoxide radicals later in the presence of water-generated hydroxyl radicals. The photo-oxidation of water takes place at the valence band in the presence of oxygen to generate hydroxyl radicals. The hydroxyl radical attacks the organic molecule and successively degrades MO and CV into less harmful products. At the same time, in the photocatalytic H<sub>2</sub> evolution reaction, the oxidation of TEOA takes place at VB, and the electrons in the CB of the NiV/NR hybrid are utilized by water to undergo reduction to evolve hydrogen.

Figure 7b shows the regeneration studies of the NiV/NR hybrid. The stability of the NiV/NR hybrid is good, and it managed to degrade 73 and 77% of MO and CV even after four cycles. The overall results of the photocatalytic reaction of the NiV/NR hybrid speak about the enhanced activity and good stability towards hydrogen evolution as well as dye degradation.

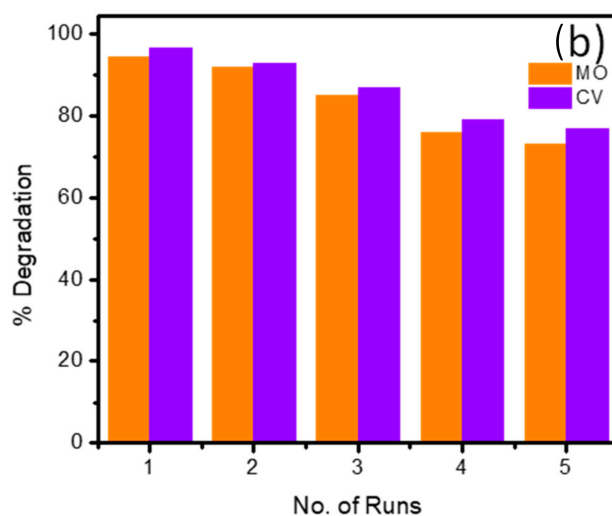
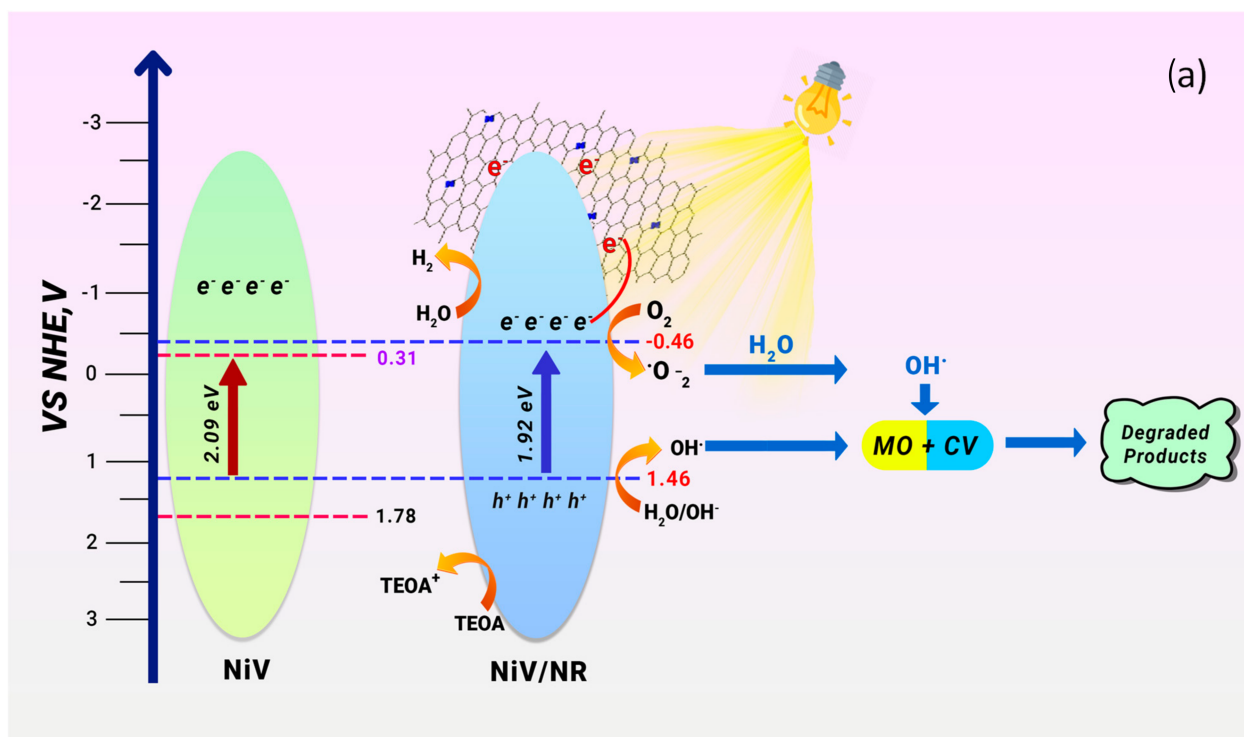


Figure 7. (a) Mechanism of photocatalysis; (b) regeneration studies.

### 3. Experimental

#### 3.1. Materials

Ammonium metavanadate and nickel chloride were purchased from Sigma Aldrich (St. Louis, MO, USA). Ethanol, sodium hydroxide, and sulfuric acid were supplied by Loba Chemie (Mumbai, India). Graphite powder, 30% ammonia, oxalic acid, and choline chloride was purchased from Fisher Scientific Ltd. (Waltham, MA, USA) and used without further treatment. Double-distilled (DI) water was used completely throughout the experiment for washing and the preparation of the solution.

#### 3.2. Synthesis of $Ni_3V_2O_8$ (NiV)

A total of 0.1 M each of ammonium metavanadate and nickel chloride were added to a mixture of ethanol and water, and the mixture was agitated for 20 min along with 7 mL of PEG-400. Following this, 1 M sodium hydroxide (50 mL) was gradually added

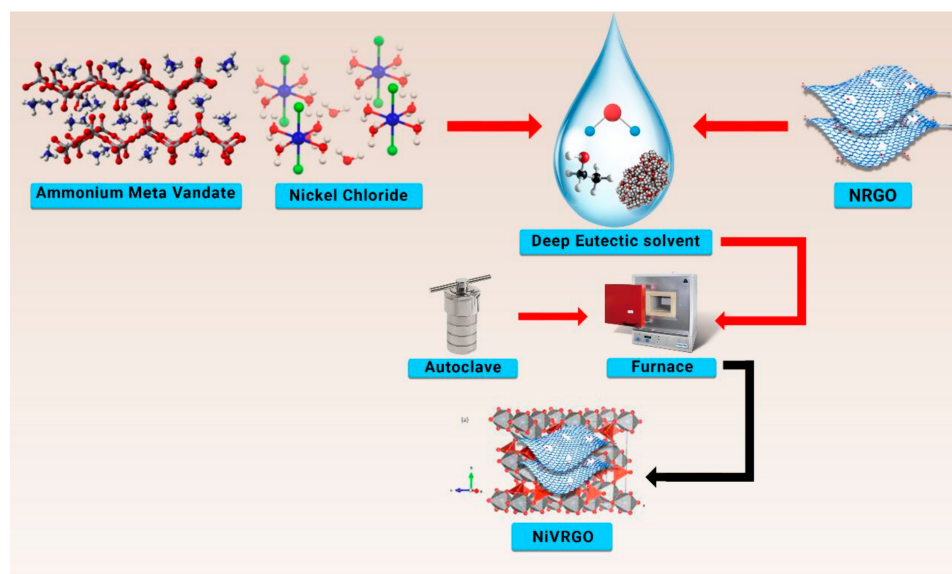
to the precursor solution, which resulted in a light green color as a product of reduction. The 100-mL autoclave, lined with Teflon, was then filled with the resulting solution for the hydrothermal treatment for 10 h at 160 °C. The product from the autoclave was cooled and rinsed with deionized water and ethanol multiple times through Whatman filter paper. Finally, the obtained  $\text{Ni}_3\text{V}_2\text{O}_8$  was collected.

### 3.3. Synthesis of NRG0

Initially, using a modified Hummer's process, the GO sheets were synthesized from graphite powder. Then, 30 mL of distilled water was added to 15 mg of GO, which was dispersed using a magnetic stirrer for five minutes and sonication for an hour. Finally, 100 mL of a 30% ammonia solution was added to the above solution as the nitrogen source. Then, a 50-mL Teflon-lined autoclave was filled with this homogenous solution and treated at 160 °C for 6 h. The collected precipitates were thoroughly washed with distilled water and ethanol three times each and then dried in a vacuum oven at 80 °C.

### 3.4. Synthesis of $\text{Ni}_3\text{V}_2\text{O}_8$ /NRGO (NiV/NR)

The deep eutectic solvent (DES) was generated from a 1:2 molar mixture of choline chloride and oxalic acid. In a beaker, the mixture was heated and stirred for 24 h at 90 °C. A 100-mL round-bottom flask containing 20 g of  $\text{ChCl}$ -oxalic acid DES was then filled with 0.015 g of NRG0 and 0.085 g of NiV and heated to 90 °C for 24 h while being magnetically stirred. The materials were separated using centrifugation (15,000 rpm) and washed five times with ethanol. Finally, the NiV/NR hybrid was obtained. The whole synthetic scheme is given in Scheme 1.



**Scheme 1.** Steps involved in the synthesis of  $\text{Ni}_3\text{V}_2\text{O}_8$ /NRGO.

### 3.5. Photocatalytic Hydrogen Evolution

An accurate amount (20 mg) of synthesized photocatalysts was taken in a quartz round-bottom flask containing 60 mL water. To the solution, 20 mL of a sacrificial agent was added, and the container was purged with nitrogen. A Xenon bulb of 300 W (Newport Corporation, Tokyo, Japan) was used as a source of light and illuminated the solution under stirring. The evolved gas was collected and measured in a gas chromatograph coupled with a thermal conductivity detector.

### 3.6. Dye Degradation Studies

Methyl orange and crystal violet were the two dyes used for degradation studies. A 300-W Xe lamp was used as a visible light source, and UV-A of 36 W (3 No.) was used as

a UV light source. A standard solution of  $100 \text{ mg L}^{-1}$  dyes was prepared and diluted as per requirement. Dyes were placed in a round bottom flask, maintained at the optimum conditions (catalyst dosage, pH), and subjected to sonication. Later, the solution was stirred continuously to attain adsorption/desorption equilibrium. At an interval of 10 min, 3 mL aliquot was collected, centrifuged, and the absorbance of the dye solution using a UV-visible spectrometer at their respective wavelengths was measured. The following Equation (1) was used to calculate the degradation percentage.

$$\text{Degradation (\%)} = \left( \frac{C_0 - C}{C_0} \right) \times 100 \quad (2)$$

where  $C_0$  is the initial concentration and  $C$  is the final concentration of the dyes, respectively.

### 3.7. Characterization

X-ray diffraction (XRD) patterns of the materials were evaluated using a Bruker D2 Phaser XRD system. For SEM and TEM analyses, the JEOL JSM 840A and JEOL/JEM 2100 were used, respectively. The X-ray photoelectron spectra were measured, and an Omicron spectrometer was used to record them. RF-6000 spectrofluorometer was used for photoluminescence studies, and the Shimadzu 1600 model was used for recording absorbance. Perkin Elmer ARNL 580C was used to measure hydrogen evolution. The electrochemical performance was studied using CHI660E, consisting of working (glassy carbon), reference (Ag/AgCl), and counter (Pt wire) electrodes.

## 4. Conclusions

A facile, environmentally friendly, and cost-effective method has been developed for the synthesis of the  $\text{Ni}_3\text{V}_2\text{O}_8/\text{NRGO}$  hybrid. The DES used in the present study improved the structural and morphological characteristics of the NiV/NR hybrid material. Enhanced activity in the NiV/NR hybrid is observed in both  $\text{H}_2$  evolution as well as dye degradation studies compared to pure NiV and NRGO. The enhanced activity could be attributed to the decreased bandgap and increased conductivity. Still, there is room for effective photocatalytic behavior of NiV through its bandgap engineering and the formation of heterostructures, etc. The synthetic method used in the present study could be a blueprint for the generation of a variety of metal vanadates and their composites for energy harvesting, conversion, storage, and environmental applications.

**Supplementary Materials:** The following supporting information can be downloaded at: <https://www.mdpi.com/article/10.3390/inorganics11020067/s1>, Figure S1. Raman spectra of NRGO, NiV and NiV/NR, Figure S2. EDS spectra of NiV/NR hybrid, Table S1: Elemental composition of NiV/NR hybrid.

**Author Contributions:** Conceptualization, F.A.A. and I.H.; Methodology, H.S.A.; Software, H.S.A.; Validation, H.S.A. and I.H.; Formal analysis, A.S.A. and H.K.A.; Investigation, A.S.A. and H.K.A.; Resources, H.K.A.; Data curation, I.H.; Writing—original draft, A.S.A.; Writing—review & editing, I.H.; Visualization, I.H.; Supervision, F.A.A., H.S.A. and I.H.; Project administration, F.A.A.; Funding acquisition, F.A.A. All authors have read and agreed to the published version of the manuscript.

**Funding:** This research received no external funding.

**Data Availability Statement:** Data is contained within the article or Supplementary Materials.

**Acknowledgments:** The authors extend their appreciation to the deputyship of Research and Innovation, Ministry of Education in Saudi Arabia for funding this research work through project number (IFKSURG-2-1327).

**Conflicts of Interest:** The authors declare no conflict of interest.

## References

1. Duan, C.; Xie, L.; Wang, S.; Dai, Y.; Yin, L. Photocatalytic hydrogen evolution by degradation of organic pollutants over quantum dots doped nitrogen carbide. *Chemosphere* **2021**, *291*, 132873. [[CrossRef](#)] [[PubMed](#)]
2. Faber, M.S.; Jin, S. Earth-abundant inorganic electrocatalysts and their nanostructures for energy conversion applications. *Energy Environ. Sci.* **2014**, *7*, 3519–3542. [[CrossRef](#)]
3. Parashuram, L.; Prashanth, M.; Krishnaiah, P.; Kumar, C.P.; Alharti, F.A.; Kumar, K.Y.; Jeon, B.-H.; Raghu, M. Nitrogen doped carbon spheres from Tamarindus indica shell decorated with vanadium pentoxide; photoelectrochemical water splitting, photochemical hydrogen evolution & degradation of Bisphenol, A. *Chemosphere* **2021**, *287*, 132348. [[CrossRef](#)]
4. Fan, Y.; Yang, R.; Zhu, R.; Zhao, H.; Lu, Q.; Chen, Z.; Hu, J. CdS-based artificial leaf for photocatalytic hydrogen evolution and simultaneous degradation of biological wastewater. *Chemosphere* **2022**, *301*, 134713. [[CrossRef](#)] [[PubMed](#)]
5. Mahala, C.; Sharma, M.D.; Basu, M. Type-II Heterostructure of ZnO and Carbon Dots Demonstrates Enhanced Photoanodic Performance in Photoelectrochemical Water Splitting. *Inorg. Chem.* **2020**, *59*, 6988–6999. [[CrossRef](#)]
6. Ren, D.; Liang, Z.; Ng, Y.H.; Zhang, P.; Xiang, Q.; Li, X. Strongly coupled 2D-2D nanojunctions between P-doped Ni<sub>2</sub>S (Ni<sub>2</sub>SP) cocatalysts and CdS nanosheets for efficient photocatalytic H<sub>2</sub> evolution. *Chem. Eng. J.* **2020**, *390*, 124496. [[CrossRef](#)]
7. Furukawa, H.; Yaghi, O.M. Storage of Hydrogen, Methane, and Carbon Dioxide in Highly Porous Covalent Organic Frameworks for Clean Energy Applications. *J. Am. Chem. Soc.* **2009**, *131*, 8875–8883. [[CrossRef](#)]
8. Liu, S.; Jiang, X.; Waterhouse, G.I.N.; Zhang, Z.M.; Yu, L.M. Efficient photoelectrocatalytic degradation of azo-dyes over polypyrrole/titanium oxide/reduced graphene oxide electrodes under visible light: Performance evaluation and mechanism insights. *Chemosphere* **2021**, *288*, 132509.
9. Karaman, C.; Karaman, O.; Show, P.-L.; Karimi-Maleh, H.; Zare, N. Congo red dye removal from aqueous environment by cationic surfactant modified-biomass derived carbon: Equilibrium, kinetic, and thermodynamic modeling, and forecasting via artificial neural network approach. *Chemosphere* **2021**, *290*, 133346. [[CrossRef](#)] [[PubMed](#)]
10. Alkorbi, A.S.; Kumar, K.Y.; Prashanth, M.; Parashuram, L.; Abate, A.; Alharti, F.A.; Jeon, B.-H.; Raghu, M. Samarium vanadate affixed sulfur self doped g-C<sub>3</sub>N<sub>4</sub> heterojunction; photocatalytic, photoelectrocatalytic hydrogen evolution and dye degradation. *Int. J. Hydrogen Energy* **2022**, *47*, 12988–13003. [[CrossRef](#)]
11. Eysseric, E.; Gagnon, C.; Segura, P.A. Uncovering transformation products of four organic contaminants of concern by photodegradation experiments and analysis of real samples from a local river. *Chemosphere* **2022**, *293*, 133408. [[CrossRef](#)] [[PubMed](#)]
12. Shah, P.; Unnarkat, A.; Patel, F.; Shah, M.; Shah, P. A comprehensive review on spinel based novel catalysts for visible light assisted dye degradation. *Process. Saf. Environ. Prot.* **2022**, *161*, 703–722. [[CrossRef](#)]
13. Prashanth, K.S.; Raghu, M.S.; Alharthi, F.A.; Sreenivasa, S.; Devi, V.S.A.; Krishnaiah, P.; Rajamma, D.B.; Akshatha, S.; Hun, J.B.; Parashuram, L. Solar light sensitive hybrid Ce<sup>4+</sup>/3<sup>+</sup> doped perovskite magnesium zirconate nano cubes for photo-catalytic hydrogen evolution and organic pollutant degradation in water. *J. Environ. Chem. Eng.* **2021**, *9*, 105364. [[CrossRef](#)]
14. Naidu, R.; Espana, V.A.A.; Liu, Y.; Jit, J. Emerging contaminants in the environment: Risk-based analysis for better management. *Chemosphere* **2016**, *154*, 350–357. [[CrossRef](#)]
15. Rizzo, L.; Malato, S.; Antakyali, D.; Beretsou, V.G.; Đolić, M.B.; Gernjak, W.; Heath, E.; Ivancev-Tumbas, I.; Karaolia, P.; Ribeiro, A.R.L.; et al. Consolidated vs new advanced treatment methods for the removal of contaminants of emerging concern from urban wastewater. *Sci. Total Environ.* **2019**, *655*, 986–1008. [[CrossRef](#)]
16. Kulkarni, A.K.; Praveen, C.S.; Sethi, Y.A.; Panmand, R.P.; Arbuj, S.S.; Naik, S.D.; Ghule, A.V.; Kale, B.B. Nanostructured N-doped orthorhombic Nb<sub>2</sub>O<sub>5</sub> as an efficient stable photocatalyst for hydrogen generation under visible light. *Dalton T.* **2017**, *46*, 14859–14868. [[CrossRef](#)]
17. Li, M.; Han, N.; Zhang, X.; Wang, S.; Jiang, M.; Bokhari, A.; Zhang, W.; Race, M.; Shen, Z.; Chen, R.; et al. Perovskite oxide for emerging photo(electro)catalysis in energy and environment. *Environ. Res.* **2022**, *205*, 112544. [[CrossRef](#)]
18. Dutta, T.; Kim, K.-H.; Uchimiya, M.; Kwon, E.E.; Jeon, B.-H.; Deep, A.; Yun, S.-T. Global demand for rare earth resources and strategies for green mining. *Environ. Res.* **2016**, *150*, 182–190. [[CrossRef](#)]
19. Wang, W.; Zhang, Y.; Huang, X.; Bi, Y. Engineering the surface atomic structure of FeVO<sub>4</sub> nanocrystals for use as highly active and stable electrocatalysts for oxygen evolution. *J. Mater. Chem. A* **2019**, *7*, 10949–10953. [[CrossRef](#)]
20. Du, X.; Zhang, X.; Li, Y.; Zhao, M. Construction of unique NiCo<sub>2</sub>S<sub>4</sub>@Ni<sub>3</sub>V<sub>2</sub>O<sub>8</sub> hierarchical heterostructures arrays on Ni foam as an efficient electrocatalyst with high stability for water oxidation. *Int. J. Hydrogen Energy* **2018**, *43*, 19955–19964. [[CrossRef](#)]
21. Liu, M.-C.; Kong, L.-B.; Kang, L.; Li, X.; Walsh, F.C.; Xing, M.; Lu, C.; Ma, X.-J.; Luo, Y.-C. Synthesis and characterization of M<sub>3</sub>V<sub>2</sub>O<sub>8</sub> (M = Ni or Co) based nanostructures: A new family of high performance pseudocapacitive materials. *J. Mater. Chem. A* **2014**, *2*, 4919–4926. [[CrossRef](#)]
22. Zhou, C.; Fan, S.; Hu, M.; Lu, J.; Li, J.; Huang, Z.; Kang, F.; Lv, R. High areal specific capacity of Ni<sub>3</sub>V<sub>2</sub>O<sub>8</sub>/carbon cloth hierarchical structures as flexible anodes for sodium—ion batteries. *J. Mater. Chem.* **2017**, *5*, 15517–15524. [[CrossRef](#)]
23. Huang, Y.; Feng, X.; Li, C.; Li, Y.; Chen, X.; Gao, X.; Chen, C.; Guang, Z.; Liu, P. Construction of hydrangea-like ZnCo<sub>2</sub>O<sub>4</sub>/Ni<sub>3</sub>V<sub>2</sub>O<sub>8</sub> hierarchical nanostructures for asymmetric all-solid-state supercapacitors. *Ceram. Int.* **2019**, *45*, 15451–15457. [[CrossRef](#)]
24. Eshaq, G.; Wang, S.; Sun, H.; Sillanpaa, M. Superior performance of FeVO<sub>4</sub>@CeO<sub>2</sub> uniform core-shell nanostructures in heterogeneous Fenton-sonophotocatalytic degradation of 4-nitrophenol. *J. Hazard. Mater.* **2020**, *382*, 121059. [[CrossRef](#)]
25. Ramavathu, L.N.; Harapanahalli, S.R.; Pernapati, N.; Tamma, B.N. Synthesis and characterization of Nickel Metavanadate (Ni<sub>3</sub>V<sub>2</sub>O<sub>8</sub>)-application as photocatalyst and supercapacitor. *Int. J. Nano Dimens.* **2021**, *12*, 411–421.

26. Suganya, B.; Chandrasekaran, J.; Maruthamuthu, S.; Saravanakumar, B.; Vijayakumar, E. Hydrothermally Synthesized Zinc Vanadate Rods for Electrochemical Supercapacitance Analysis in Various Aqueous Electrolytes. *J. Inorg. Organomet. Polym. Mater.* **2020**, *30*, 4510–4519. [[CrossRef](#)]
27. Vesali-Kermani, E.; Habibi-Yangjeh, A.; Ghosh, S. Efficiently enhanced nitrogen fixation performance of g-C<sub>3</sub>N<sub>4</sub> nanosheets by decorating Ni<sub>3</sub>V<sub>2</sub>O<sub>8</sub> nanoparticles under visible-light irradiation. *Ceram. Int.* **2020**, *46*, 24472–24482. [[CrossRef](#)]
28. Zheng, J.; Zhang, L. One-step in situ formation of 3D hollow sphere-like V<sub>2</sub>O<sub>5</sub> incorporated Ni<sub>3</sub>V<sub>2</sub>O<sub>8</sub> hybrids with enhanced photocatalytic performance. *J. Hazard. Mater.* **2021**, *416*, 125934. [[CrossRef](#)]
29. Kumar, K.Y.; Saini, H.; Pandiarajan, D.; Prashanth, M.; Parashuram, L.; Raghu, M. Controllable synthesis of TiO<sub>2</sub> chemically bonded graphene for photocatalytic hydrogen evolution and dye degradation. *Catal. Today* **2018**, *340*, 170–177. [[CrossRef](#)]
30. Asgari, S.; Ziarani, G.M.; Badiei, A.; Setayeshmehr, M.; Kiani, M.; Pourjavadi, A. Electrospun Ag-decorated reduced GO-graft-chitosan composite nanofibers with visible light photocatalytic activity for antibacterial performance. *Chemosphere* **2022**, *299*, 134436. [[CrossRef](#)]
31. Arumugam, M.; Lee, S.J.; Begildayeva, T.; Naik, S.S.; Yu, Y.; Lee, H.; Theerthagiri, J.; Choi, M.Y. Enhanced photocatalytic activity at multidimensional interface of 1D-Bi<sub>2</sub>S<sub>3</sub>@2D-GO/3D-BiOI ternary nanocomposites for tetracycline degradation under visible-light. *J. Hazard. Mater.* **2021**, *404*, 123868. [[CrossRef](#)] [[PubMed](#)]
32. Kumar, K.Y.; Prashanth, M.; Parashuram, L.; Palanivel, B.; Alharti, F.A.; Jeon, B.-H.; Raghu, M. Gadolinium sesquisulfide anchored N-doped reduced graphene oxide for sensitive detection and degradation of carbendazim. *Chemosphere* **2022**, *296*, 134030. [[CrossRef](#)]
33. Karmakar, A.; Srivastava, S.K. In situ fabricated nickel vanadate/N-doped reduced graphene oxide hybrid as an advanced electrocatalyst in alkaline hydrogen evolution reaction. *J. Mater. Chem. A* **2019**, *7*, 15054. [[CrossRef](#)]
34. Arumugam, S.; Bavani, T.; Preeyanghaa, M.; Alaswad, S.O.; Neppolian, B.; Madhavan, J.; Murugesan, S. A facile synthesis of visible light driven Ni<sub>3</sub>V<sub>2</sub>O<sub>8</sub> nano-cube/BiVO<sub>4</sub> nanorod composite photocatalyst with enhanced photocatalytic activity towards degradation of acid orange 7, Chemosphere. *Chemosphere* **2022**, *308*, 136100. [[CrossRef](#)] [[PubMed](#)]
35. Li, Y.; Duan, F.; Liu, S.; Peng, C. Hierarchical flower-like Ni<sub>3</sub>V<sub>2</sub>O<sub>8</sub>/Co<sub>3</sub>V<sub>2</sub>O<sub>8</sub> composites as advanced anode materials for lithium-ion batteries. *Funct. Mater. Lett.* **2020**, *13*, 2050014. [[CrossRef](#)]
36. Yang, M.; Fu, X.; Zhang, J.; Wang, Z.; Wang, B.; He, L.; Wu, Z.; Cheng, H.; Pan, H.; Lu, Z. Hierarchical ultrafine Ni<sub>3</sub>V<sub>2</sub>O<sub>8</sub> nano-particles anchored on rGO as high-performance anode materials for lithium-ion batteries. *Energy Technol.* **2019**, *7*, 1800784.
37. Yu, X.; Zhang, J.; Zhang, J.; Niu, J.; Zhao, J.; Wei, Y.; Yao, B. Photocatalytic degradation of ciprofloxacin using Zn-doped Cu<sub>2</sub>O particles: Analysis of degradation pathways and intermediates. *Chem. Eng. J.* **2019**, *374*, 316–327. [[CrossRef](#)]
38. Chen, F.; Yang, Q.; Li, X.; Zeng, G.; Wang, D.; Niu, C.; Zhao, J.; An, H.; Xie, T.; Deng, Y. Hierarchical assembly of graphene-bridged Ag<sub>3</sub>PO<sub>4</sub>/Ag/BiVO<sub>4</sub> (040) Z-scheme photocatalyst: An efficient, sustainable and heterogeneous catalyst with enhanced visible-light photoactivity towards tetracycline degradation under visible light irradiation. *Appl. Catal. B Environ.* **2017**, *200*, 330–342. [[CrossRef](#)]
39. Zhao, X.; Lu, Z.; Ma, W.; Zhang, M.; Ji, R.; Yi, C.; Yan, Y. One-step fabrication of carbon decorated Co<sub>3</sub>O<sub>4</sub>/BiVO<sub>4</sub> p-n heterostructure for enhanced visible-light photocatalytic properties. *Chem. Phys. Lett.* **2018**, *706*, 440–447. [[CrossRef](#)]
40. Chen, F.; Yang, Q.; Sun, J.; Yao, F.; Wang, S.; Wang, Y.; Wang, X.; Li, X.; Niu, C.; Wang, D.; et al. Enhanced Photocatalytic Degradation of Tetracycline by AgI/BiVO<sub>4</sub> Heterojunction under Visible-Light Irradiation: Mineralization Efficiency and Mechanism. *ACS Appl. Mater. Interfaces* **2016**, *8*, 32887–32900. [[CrossRef](#)]
41. Wang, B.; Zhang, J.; Huang, F. Enhanced visible light photocatalytic H<sub>2</sub> evolution of metal-free g-C<sub>3</sub>N<sub>4</sub>/SiC heterostructured photocatalysts. *Appl. Surf. Sci.* **2017**, *391*, 449–456. [[CrossRef](#)]
42. Jing, L.; Xu, Y.; Huang, S.; Xie, M.; He, M.; Xu, H.; Li, H.; Zhang, Q. Novel magnetic CoFe<sub>2</sub>O<sub>4</sub>/Ag/Ag<sub>3</sub>VO<sub>4</sub> composites: Highly efficient visible light photocatalytic and antibacterial activity. *Appl. Catal. B Environ.* **2016**, *199*, 11–22. [[CrossRef](#)]
43. Rafique, M.; Hamza, M.; Shakil, M.; Irshad, M.; Tahir, M.B.; Kabli, M.R. Highly efficient and visible light-driven nickel-doped vanadium oxide photocatalyst for degradation of Rhodamine B Dye. *Appl. Nanosci.* **2020**, *10*, 2365–2374. [[CrossRef](#)]
44. Ranjana, R.; Rakshit, A.; Suresh, C.A. Role of nickel vanadate in photocatalytic degradation of azure a. *J. Curr. Chem. Pharm. Sc.* **2014**, *4*, 157–163.

**Disclaimer/Publisher's Note:** The statements, opinions and data contained in all publications are solely those of the individual author(s) and contributor(s) and not of MDPI and/or the editor(s). MDPI and/or the editor(s) disclaim responsibility for any injury to people or property resulting from any ideas, methods, instructions or products referred to in the content.